

Integrated Design Methodology for Advanced Functional Materials

Denis Kramer*, Adrian Fortuin,
Jiangming Cao, Aleena Anna
Thomas
*Helmut-Schmidt-University
Hamburg / University of the
Armed Forces
Hamburg, Germany
d.kramer@hsu-hh.de

Claudio Pistidda*, Thi Thu Le,
Thomas Klassen
*Helmholtz-Zentrum Hereon,
Institute for Hydrogen
Technology
Geesthacht, Germany
claudio.pistidda@hereon.de

Daniel Höche*, Min Deng
*Helmholtz-Zentrum Hereon,
Institute for Surface Science
Geesthacht, Germany
daniel.hoeche@hereon.de

Michael Störmer*, Gnanavel
Vaidhyanathan Krishnamurthy
*Helmholtz-Zentrum Hereon,
Institute for
Photoelectrochemistry
Geesthacht, Germany
michael.stoermer@hereon.de

Abstract – Engineering innovation and technological leadership increasingly depend on the timely availability of advanced functional materials. Development times of technology enabling materials, however, are still typically measured in decades. Within the Digital Materials Foundry, we develop and implement an integrated design methodology that equally draws on advanced high-throughput quantum mechanical simulations and automated combinatorial synthesis to dramatically accelerate the optimization of materials for a range of energy applications. Here we present our recent infrastructure advances as well as selected initial results from our research on hydrogen storage materials, meta-materials, magnesium batteries, and magneto-electrocatalysis.

Materials Design, Density Functional Theory, Physical Vapour Deposition, Hydrogen Storage, Meta-Materials, Electrocatalysis.

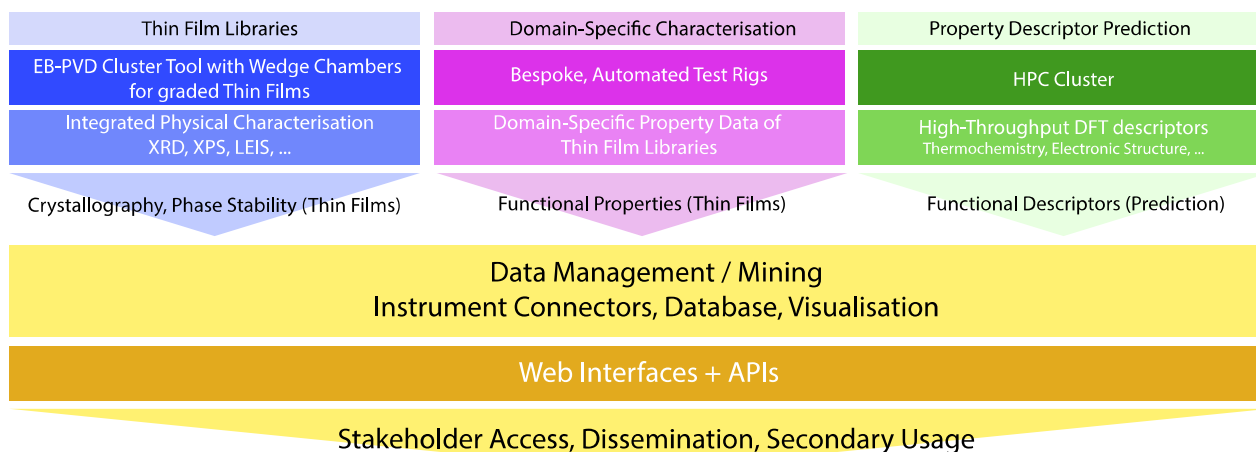
I. INTRODUCTION

“Classical” Materials Science is not fit for the accelerated development cycles of the future. Traditionally, materials breakthroughs are often sparked by serendipitous discovery followed by many years of development and optimisation. For instance, the fundamental chemistry that enabled the recent advent of Li-Ion batteries was demonstrated by John Goodenough in 1980 [1], but it took eleven years for the first

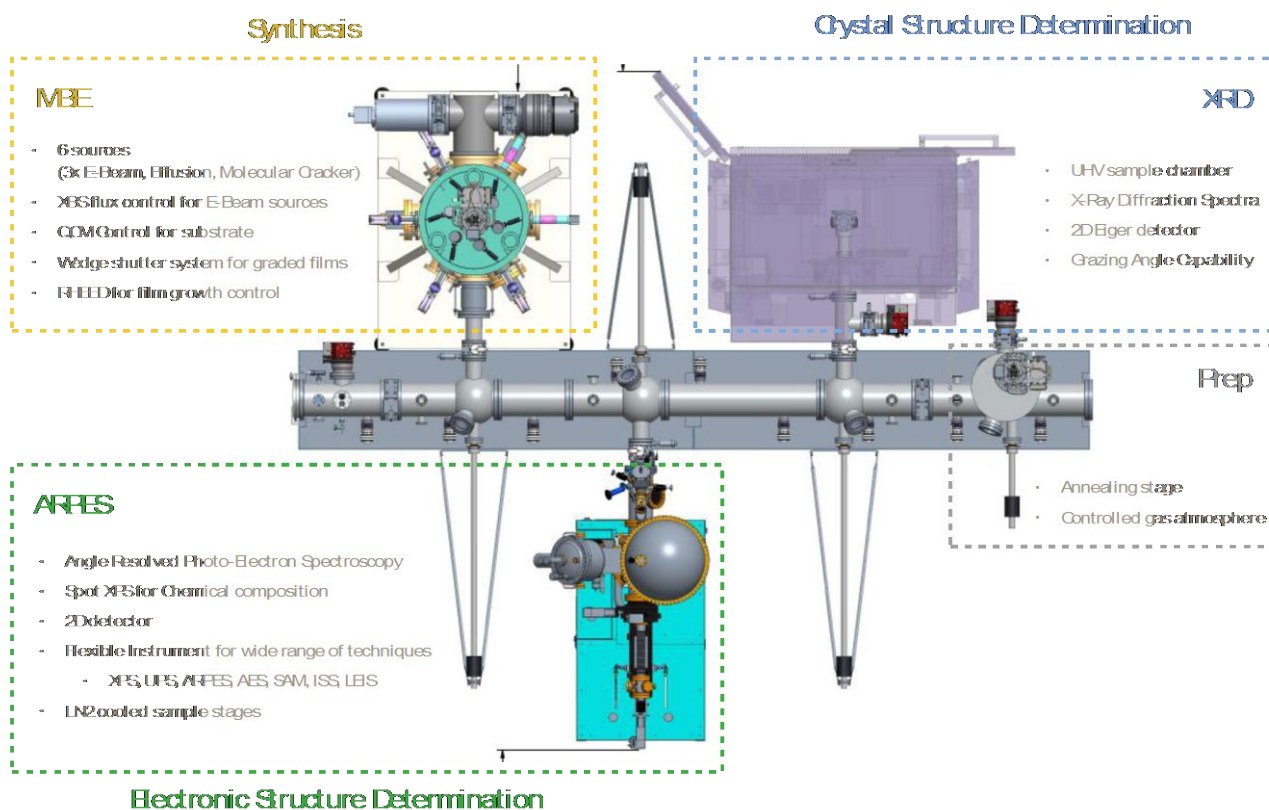
commercial application in consumer electronics by Sony in 1991 and almost 40 years for Li-Ion batteries to scale to high energy applications such as electric vehicles. Similarly, high surface area Pt oxygen reduction catalysts—now used in fuel cell cars—were already known in the 1960 [2], but it took almost 40 years to develop the fundamental understanding [3] to enable the rational development of Pt alloy catalysts around 2000 [4] that ultimately were utilised in Toyota’s 2014 Mirai; a staggering 50+ years later!

Two major paradigm shifts are underway in Materials Science that promise to significantly speed-up development and shorten times to commercialisation: (1) truly predictive *Computational Materials Design* (CMD) based on advanced and efficient quantum mechanical methods is now possible, and an impressive array of *functional descriptors* can be computed fully *in silico*, allowing for almost cost-free scaling of discovery/optimisation once a valid and computable descriptor is identified. (2) *Combinatorial Materials Science* (CMS) now allows it to synthesis materials libraries across chemical spaces with unprecedented speed followed by automated characterisation.

Whilst CMD and CMS are impressive methodological advancements, they both have shortcomings and difficulties



FIGURES 1: PILLARS OF THE INTEGRATED MATERIALS DESIGN PLATFORM COMPRISING ADVANCED SYNTHESIS, CHARACTERIZATION AND MODELLING.



FIGURES 2: PHYSICAL VAPOR DEPOSITION CLUSTER TOOL FOR THE DEPOSITION OF CHEMICALLY-GRADED THIN FILM LIBRARIES WITH INTEGRATED ANALYTICS FOR CRYSTAL STRUCTURE DETERMINATION AND ADVANCED X-RAY SPECTROSCOPY.

that need to be addressed to unlock their full potential. Interestingly, challenges are often complementary promising significant benefit from close coupling between CMD and CMS. This, however, has not yet happened in general, partially because the interdisciplinary nature and the needed disparate skillsets have led to distinct scientific communities that only now start to talk to each other.

II. METHODOLOGY

There is a clear opportunity for technological advance by exploiting the benefits of a fully integrated, digitised materials design methodology that equally draws on computational and combinatorial methodologies linked by a common data management and data mining platform. Such a platform has to comprise three pillars (cf. FIGURE 1): (1) combinatorial synthesis and characterisation of materials libraries, (2) modular, application-focused testing and screening of materials libraries, and (3) predictive modelling of materials properties in high-throughput mode, all feeding into sophisticated informatics for data management, visualisation and processing to bring things together.

A. Combinatorial synthesis

The ideal synthesis strategy has to be versatile, fast, reproducible and ideally yields materials systems that closely align with application environments. Especially, the demand for versatility and application relevance often leads to conflicts and necessary compromises.

Within the Digital Materials Foundry, we champion thin-film libraries synthesised by Physical Vapour Deposition (PVD) as model systems, because they allow for fast and reliable synthesis of an exceptionally broad spectrum of

materials as well as standardised characterisation. The foundries unique combinatorial thin-film synthesis platform with integrated x-ray spectroscopy and diffraction is depicted in FIGURE 2. The platform is designed to synthesise metals, alloys, oxides and corrosive chemistries such as sulphides and other transition metal dichalcogenides as well as mixtures of these compounds. The platform comprises (1) a combinatorial physical vapor deposition chamber with six sources, (2) a preparation chamber for post-treatment of deposited films, (3) an x-ray spectrometer for elemental analysis and electronic structure determination, and (4) an x-ray diffractometer for crystal structure determination of deposited films.

The entire system is designed to operate in ultra-high vacuum (UHV) realising the demanding environment for molecular beam epitaxy (MBE). Although we do not generally aim for single crystal films, the cleanliness, purity and stoichiometric precision associated with MBE are of utmost importance. Films are deposited on two-inch wafer substrates with up to six sources with individual flux control allowing to vary stoichiometry during deposition; and adjustable substrate shutters allow to mask varying areas during deposition to create chemically graded films. Hence, a single wafer can carry a library of tens if not hundreds of stoichiometries. The setup comprises three e-beam evaporators to deposit metals, a molecular cracker to provide atomic H, O, and N, and specialised sources for S, C, and P. Due to this variety of sources, almost the entire periodic table from H to Au is available (excluding noble gases). Finally, the system is easily extendable with additional sources such as magnetrons or effusion cells to fulfil future needs.

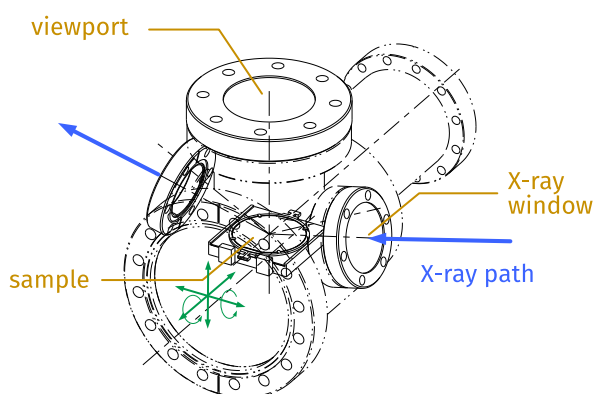
Deposited films can be annealed in a separate preparation chamber under controlled atmosphere to ensure well crystallised films with the controlled gas atmosphere providing additional means to control chemical composition as well as film morphology [5].

B. Physical Characterisation

Understanding the physical properties of deposited films is crucial to map out structure-property relationships. The platform, therefore, integrates two sophisticated analytical tools within the UHV environment: (1) an X-ray spectrometer for determining stoichiometry and electronic structure and (2) an X-ray diffractometer to determine crystal structure. To the best of our knowledge, the integration of both within one UHV environment is a unique feature enabling comprehensive characterisation of even highly reactive materials, because it eliminates any chance of contamination or degradation during transfers.

The x-ray spectrometer, developed and manufactured by Specs, ensures the ability to confirm stoichiometry of synthesised films via X-ray photoelectron spectroscopy (XPS). Elemental composition is determined by analysing the energy spectrum of released photoelectrons with each element providing a characteristic spectrum [6]. Substrates are mounted on an UHV manipulator, which enables lateral translations to scan across the entire area of the two-inch wafers for spot characterisation of composition across chemically graded films. The X-ray spectrometer also comprises a low-energy X-ray source and angle-resolved detector to study the electronic structure of valence electrons close to the Fermi level. Angle-resolved photo-electron spectroscopy (ARPES) provides highly valuable experimental access to the electronic structure of compounds that defines their chemical (and optical) reactivity and provides a direct experimental twin to band structure calculations—promising direct experimental validation of predictions even for electronically challenging compounds such as strongly correlated oxides.

Finally, the platform incorporates a x-ray diffractometer (XRD) within the UHV environment. A highly customised Bruker D8 Discover diffractometer is developed to house an UHV measurement chamber with manipulator and pass a UHV transfer arm through the back of the diffractometer. This novel prototype design developed with Bruker enables the measurement of X-ray diffractograms without samples ever leaving the UHV environment. The sample chamber design



FIGURES 3: UHV SAMPLE CHAMBER FOR X-RAY DIFFRACTION STUDIES WITH X-RAY WINDOW AND MOVABLE SAMPLE STAGE.



FIGURES 4: RAMAN MEASUREMENT SETUP FOR AIR-TIGHT THIN-FILM SAMPLES: (A, B) RAMAN CELL, (C) SET UP OF RAMAN MEASUREMENT

(cf. FIGURE 3) incorporates two x-ray windows to pass the X-ray beam from the source to the sample and scattered X-rays back to the detector, which both are housed outside the UHV environment. The sample stage is mounted onto a manipulator that allows to translate and rotate the sample to align the thin films and scan the x-ray spot across the entire two-inch wafers, enabling local determination of the crystal structure. The need for five axis manipulation (three translations, two rotations) implies challenges for the manipulator design compounded by the limited space to host the manipulator within the XRD enclosure. This has been overcome by a combination of expanding the XRD enclosure and developing a highly compact manipulator design.

C. Domain-specific characterisation

Thin films provide model systems to gauge materials properties in well-controlled and—to some degree—simplified experimental setups. They allow to estimate relevant properties of materials for a given application, but rarely provide quantitative measures that exactly match performance under application conditions. They are a highly useful intermediary systems to quickly identify “hotspots” in phase space but require bespoke measurement setups. Because these setups are necessarily application-specific, a modular strategy is attractive, where an array of independent experimental platforms is available utilising standardised thin film substrates.

Raman holders (cf. FIGURE 4A,B) are used to measure *in-situ* thin hydride films under different H_2 pressures (10^{-2} bar – 15 bar) and temperatures (-60 °C – 500 °C). By using an *in-house* built *ex-situ* Raman cell (cf. FIGURE 4B), samples with dimensions up to 2×2 inches produced by PVD can be investigated. All Raman measurements (*in-situ* and *ex-situ*) are carried out using a WITec confocal Raman microscope (Alpha300 R) equipped with 523 nm and 633 nm lasers (cf. FIGURE 4C).

A multi-electrode electrochemical cell is designed for high throughput screening of alloy-type anode materials for Mg-ion batteries (MIB). The cell enables simultaneous electrochemical measurements, like cyclic voltammetry (CV), of micro-anodes in the thin film array (e.g. 4×4) manufactured by PVD. A three-electrode system is utilised for the electrochemical study in conventional non-corrosive Mg battery electrolytes (e.g. 0.5 M $Mg(ClO_4)_2$ in acetonitrile (I)). An Ag wire is used as the quasi-reference electrode (QRE). The stability of the potential of the Ag wire with time in Mg battery electrolytes can be examined with an internal reference such as the ferrocene/ferrocenium (Fc/Fc^+) couple, which shows negligible redox change in organic solutions [7].

D. High-Throughput Materials Modelling

Ab initio modeling, based on Density-Functional-Theory (DFT), has matured into a highly predictive theory to gauge a very wide range of materials properties. Fundamental properties such as phase stability, electronic structure and

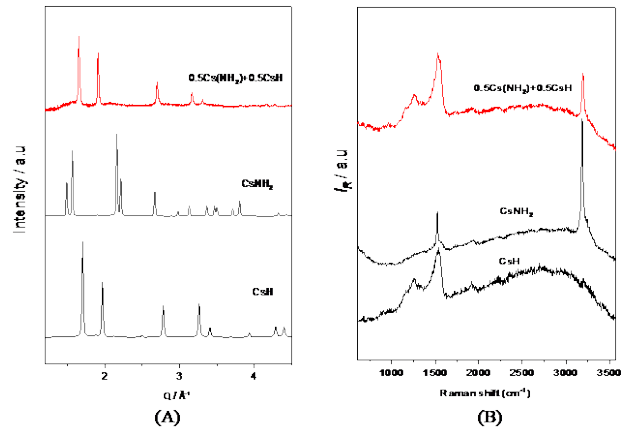
thermo-chemistry have become routine calculations that can be fully automated [8]. In addition, properties such as ion mobility or surface reactivity that require more advanced calculations are increasingly encapsulated within automated workflows promising similar levels of automation and scaling in the near future.

We actively develop our digital infrastructure, which consists of a selection of third-party codes combined by in-house “glue codes” that manage computations and data storage and processing, complemented by a visualisation layer. We strongly rely on a small set of mature DFT codes to predict materials properties [9]. DFT calculations are managed with the “atomate” framework [10] allowing for automated computation of pre-defined workflows and sophisticated error handling. Through in-house codes, this HT-DFT layer is coupled with advanced search strategies to explore phase space. Commonly, this takes the form of heuristics or statistic models that we construct from a limited set of DFT calculations spanning the chemical space of interest [11]. For even more advanced searches, we construct model Hamiltonians that capture the physics of that particular chemical space, but compute orders of magnitude faster than DFT to drive Monte Carlo or even brute force explorations of phase space. For instance, we often utilise cluster expansions and the CASM code [12] to efficiently map the energy landscape of substitutional disorder in a given host structure.

III. APPLICATIONS

A. Hydrogen storage

Amide-hydride-based materials, such as $\text{LiNH}_2\text{-LiH}$ [13], and $\text{Mg}(\text{NH}_2)_2\text{-2LiH}$ [14] are considered potential hydrogen storage candidates for mobile and stationary applications owing to their high hydrogen storage capacity and favourable thermodynamics, which in many cases allow the reversible release of hydrogen at temperatures below 150 °C. However, one of the main problems of amide-hydride systems is the sluggish dehydrogenation/re-hydrogenation kinetics, which limits their practical applications. It has been found that the formation of reaction intermediates such as hydride-amide solid solutions might influence the material properties. Among the recently discovered amide-hydride solid solutions are $\text{Li}_{2-x}\text{NH}_{1+x}$, $\text{K}(\text{NH}_2)_x\text{H}_{1-x}$, $\text{Rb}(\text{NH}_2)_x\text{H}_{1-x}$ in $\text{LiNH}_2\text{-LiH}$, $\text{KNH}_2\text{-KH}$, and $\text{RbNH}_2\text{-RbH}$ systems, respectively. These solid solutions are formed by the exchange of amide/hydride anions at the amide/hydride interface. The substitution of anion species taking place at the interfaces is suggested to facilitate ionic transport in these systems. Similar to the systems $\text{KNH}_2\text{-KH}$ [15] and $\text{RbNH}_2\text{-RbH}$ [16], a mixed cation amid-hydride solid solution is likely to be formed in the system $\text{CsNH}_2\text{-CsH}$. To verify this hypothesis, initial tests were performed. According to XRD data (cf. FIGURE 5A), the diffraction reflection of a single cubic phase, which has a similar structural geometry as the CsH , is visible for the 1:1 composition. Besides, Raman spectra (cf. FIGURE 5B), exhibit a shift to higher frequencies of the N-H bond, signifying a substitution of H^- and $[\text{NH}_2]^-$ in the 1:1 composition. As shown in FIGURE 6, the unit cell of the solid solution expands with the increase in amide amount, indicating the $[\text{NH}_2]^-/\text{H}^-$ substitution taking place between amide and hydride. Lattice parameters obtained experimentally by Rietveld refinement agree well with Vegard’s law, suggesting an ideal behaviour for the solid solution ($\Delta H_{\text{mix}} \sim 0$, and $\Delta V_{\text{mix}} \sim 0$). In the next step, the formation of the solid solution will be assessed by proton double quantum experiments (^1H 2D SS MAS NMR)



FIGURES 5: (A) XRD PATTERNS AND (B) RAMAN SPECTRA OF THE STARTING AND MIXED HYDROGEN STORAGE MATERIALS.

and subsequently evaluated by theoretical studies via *First Principles* calculations (e.g. nuclear spin-spin coupling). The combination of experimental evidence and theoretical predictions could provide an appropriate way for predicting and assessing the structural properties of the material.

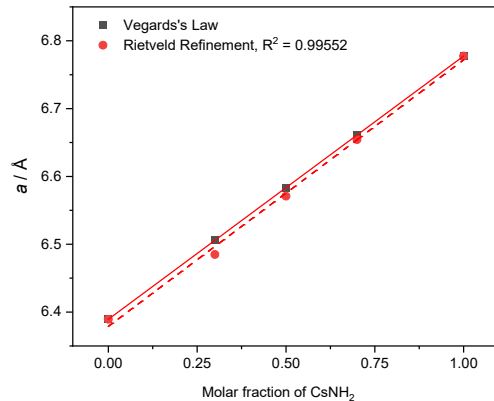


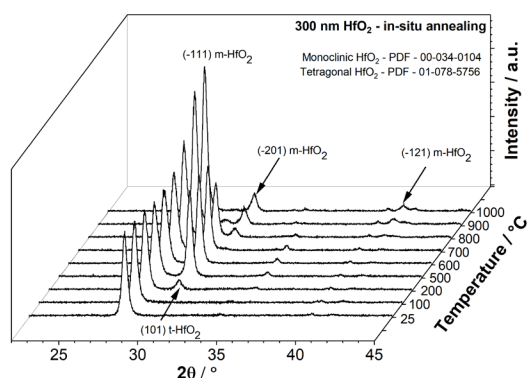
FIGURE 6: UNIT CELL PARAMETERS OF THE $\text{Cs}(\text{NH}_2)_x\text{H}_{1-x}$ SOLID SOLUTION AS A FUNCTION OF THE AMIDE FRACTION OBTAINED FROM RIETVELD REFINEMENT OF THE XRD DATA AND VEGARD’S LAW.

B. Metamaterials

A selective emitter can enhance the efficiency of a thermophotovoltaic (TPV) system by suppressing radiation above the cut-off wavelength of a low bandgap photovoltaic (PV) cell [17]. Unfortunately, there exists no material in nature that shows selective emission. A thin-film metamaterial containing alternate layers of a metal and a dielectric in the nanometre scale, however, can be artificially fabricated to engineer selective emitters [18]. The selective emitter functions like a blackbody, and it needs to operate at temperatures above 1000 °C for a long-time posing challenges for durability. Therefore, refractory materials like W and HfO_2 are best suited for thermophotovoltaic applications.

At high working temperatures above 1000 °C, thermally activated degradation processes like diffusion, oxidation and phase transformation come into play. FIGURE 7 shows in-situ annealed diffractograms of a single 300 nm thick HfO_2 layer from room temperature up to 1000 °C. The as-prepared HfO_2 film contains two phases, a monoclinic and an amorphous phase. On heating the layer to 200 °C, the amorphous phase first transforms into the tetragonal phase, and upon further

heating above 800 °C, the tetragonal phase transforms into the stable monoclinic phase [19]. At 1000 °C, the entire film exists only in the monoclinic phase with no reverse phase transformation observed on cooling down. A phase change from tetragonal to monoclinic structure increases the unit cell volume by 3.7%. In order to accommodate the volume change, voids are generated in the HfO₂ layer.

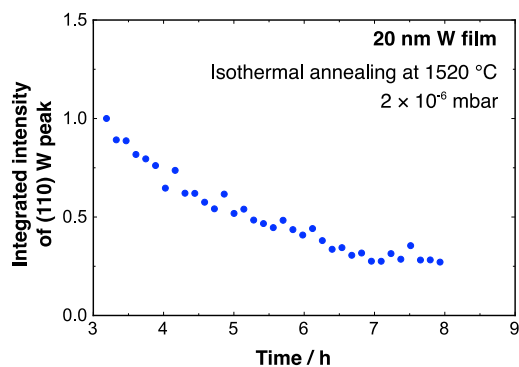


FIGURES 7: DIFFRACTOGRAMS OF AN IN-SITU ANNEALED 300 NM SINGLE HfO₂ LAYER FROM 25 °C UP TO 1000 °C AT 3×10^{-6} MBAR. AT 200 °C, A NEW (101) TETRAGONAL HfO₂ PHASE EMERGES AT 30.3°. ON FURTHER REACHING 800 °C, THE (101) TETRAGONAL PEAK VANISHES AND ONLY PEAKS FROM MONOCLINIC HfO₂ (-111), (-201) AND (-121) ARE VISIBLE AT 1000 °C.

A 20 nm single tungsten layer has a bcc crystal structure, and the thermal stability was validated by an in-situ isothermal annealing experiment at 1520 °C for 6 h at 3×10^{-6} mbar. The integrated intensity of the XRD diffraction pattern correlates with the volume fraction of a phase in the material. Here, the normalised integrated intensity of the (110) bcc tungsten peak as a function of time as shown in FIGURE 8 is used. A gradual drop in intensity is observed due to the loss of scatterers from the film, as tungsten gets oxidised by residual oxygen present in the atmosphere of the annealing chamber [19]. The formed tungsten oxide sublimates rapidly at such high temperatures. Future work is aimed toward utilizing the PVD cluster tool to prepare dielectric layers with a stable phase and dope the metallic layers to improve the oxidation resistance and durability in the multilayer stack.

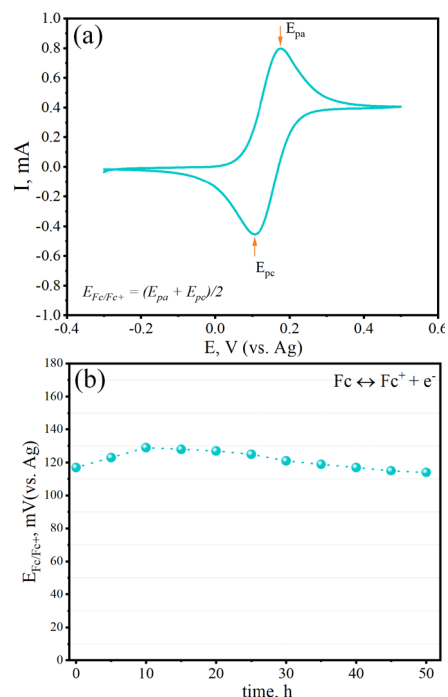
C. Magnesium batteries

The adoption of alloy-type anodes (like Mg₃Bi₂ [20]) for magnesium ion batteries (MIB) could bypass the passivation issue in conventional non-corrosive electrolytes, which have



FIGURES 8: THE INTEGRATED INTENSITY OF (110) W PEAK IN A 20 NM SINGLE LAYER AS A FUNCTION OF TIME DURING ISOTHERMAL ANNEALING AT 1520 °C AND 3×10^{-6} MBAR. A GRADUAL DROP IN INTENSITY IS OBSERVED AS A RESULT OF LOSS IN THE FILM, DUE TO OXIDATION TUNGSTEN AND LAYER SUBLIMATION OF VOLATILE TUNGSTEN OXIDES.

good compatibility with some high voltage/high capacity cathode materials. The combination of alloy-type anodes, non-corrosive conventional electrolytes and suitable cathode materials could be a new way for next-generation high-performance MIB, providing high capacity alloy anodes that can work properly in conventional electrolytes. This platform enables the fast and reliable synthesis of diverse alloy-type



FIGURES 9: (A) CV CURVES OBTAINED IN 0.5 M Mg(ClO₄)₂/ACN SOLUTION CONTAINING 0.05 M Fc WITH Pt WORKING ELECTRODE, ACTIVATED CARBON CLOTH COUNTER ELECTRODE AND Ag WIRE REFERENCE ELECTRODE; (B) STABILITY OF E_{Fc/Fc+} VS. Ag WITH TIME.

anode thin films via PVD and functional screening based on high throughput electrochemical measurements. However, before the implementation of this methodology, a reference electrode that can work reliably in conventional MIB electrolytes is required to ensure accurate electrochemical testing. Widely adopted Mg foils cannot be utilised in this scenario due to the passivation of pure Mg metal in conventional electrolytes. Ag wire, as a common alternative quasi-reference electrode (QRE), could be a good candidate, but the stability of its potential in the electrolytes of interest has to be demonstrated.

The Fc/Fc⁺ redox couple has a consistent redox potential in diverse organic solutions [21]. Therefore, it can be used as an internal standard reference for examining the stability of Ag wires when serving as a QRE. The redox potential of Fc/Fc⁺ versus Ag QRE (E_{Fc/Fc+} vs. Ag) can be determined from the CV curve obtained in 0.5 M Mg(ClO₄)₂/I solution containing 0.05 M Fc with a Pt working electrode, activated carbon cloth counter electrode and Ag reference electrode (cf. FIGURE 9A). On this basis, the stability of E_{Fc/Fc+} vs. Ag with time represents the stability of the Ag QRE in the electrolyte. FIGURE 9B shows the variation of E_{Fc/Fc+} vs. Ag with time, indicating a potential shift of around 20 mV within 50h, which is sufficiently small for the short-time electrochemical measurements employed during the fast screening of anode materials.

The hardness of an Ag wire (e.g. with 0.5 mm diameter) allows it to be a freestanding reference electrode. The

combination of a Pt wire counter electrode and an Ag wire reference electrode enables easy assembly of the multi-electrode electrochemical testing cell. In the next stage, the compositionally graded thin film array manufactured by PVD will be characterised via the electrochemical testing rig consisting of the multi-electrode cell and a multi-channel potentiostat. Composition-dependant Mg plating/stripping reversibility and cycling stability of the anode materials will be evaluated. Data will be adopted for data mining and the construction of digital design maps based on Density-Functional-Theory (DFT) and other modelling tools.

D. Magneto-Electrocatalysis

Utilising interactions with magnetic fields is an increasingly popular approach in materials science. This provides a novel opportunity to change the energy landscape during material synthesis. In heterogeneous catalysis, this promises materials that catalyse alternative mechanistic pathways for reactions of interest, e.g., the oxygen evolution reaction (OER) in water electrolysis.

One approach is to apply a strong magnetic field *in-situ* using ferro- and para-magnetic materials during OER [22]. Due to the bulk electron spin alignment, the additional magnetic field may provide a pathway to crystallising materials that can exist in different electronic states. For example, Co^{3+} has six electrons occupying its *d*-orbitals. In an octahedral configuration, these electrons can occupy a low spin (LS) state where they fill all three t_{2g} orbitals. Alternatively, a high spin (HS) state can be synthesized, where one electron occupies each of the three t_{2g} orbitals and the two e_g orbitals, with the remaining electron spin-pairing the electron in the lowest energy orbital [23]. In the example of Co^{3+} , the LS configuration has a $\mu_s = 0$ and the HS configuration has a $\mu_s = 4$, where μ_s is the magnetic moment in units of Bohr's magneton. Hence, only the HS state can energetically couple with an external magnetic field. The significance of different crystal spin states are: (i) HS states usually lead to larger lattice constants and (ii) it interacts with adsorbates differently due to differences in orbital bonding.

We carried out *First Principles* calculations of the total energy for the $\text{CoO}(\text{OH})$ system, using the generalized-gradient-approximation to Density Functional Theory (DFT) as parameterized by Perdew and Wang [24]. The Kohn-Sham orbitals are expanded in a plane-wave basis with a cutoff of $E_{\text{cutoff}} = 520$ eV. The electronic density was computed self-consistently until the variation was below the threshold of 10^{-6}

eV. Spin-polarised calculations are performed on a $2 \times 2 \times 1$ supercell with μ_s explicitly initialised as $\mu_s = 0$ for LS Co^{3+} . The position of the ions in the unit cell were relaxed until the residual forces were below the threshold of 10^{-2} eV \AA^{-1} . A Hubbard U correction was applied to Co as described by the Materials Project [8] with $U = 3.32$ eV. Calculations were repeated by initialising $\mu_s = 4$ for an increasing number of Co atoms at random, until the HS state was reached.

The preliminary results are presented in FIGURE 10. As expected, the HS state occupies a larger lattice volume. The energy difference is on the order of 1 eV per Co atom between LS and HS states. A quadratic equation can be fitted to the calculated energy, indicating that next-neighbour interactions are relevant and need to be captured by a model Hamilton. Monte Carlo methods can then be used to quantify lateral interactions between spin states through pair correlation functions. Because it is unlikely that realistic magnetic fields can overcome an energy penalty of 1 eV by themselves, our interest currently shifts to the exchange-coupled decay length of a HS state and whether it is comparable with nanometre thick surface layers to provide an alternative explanation for experimental observations.

IV. CONCLUSION AND OUTLOOK

We are well advanced with our aim to implement a powerful and unique integrated platform to accelerate materials design for energy applications. Each of the three pillars is progressing: (1) the PVD cluster tool design is completed and currently in manufacturing, (2) the first set of domain-specific test rigs produces initial results, and (3) we have successfully transitioned our computational infrastructure to the new HSUPer platform [25] with work ongoing to integrate a large-scale data repository.

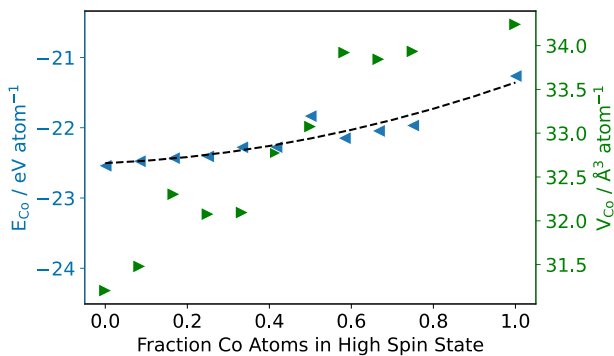
In the next phase, we look forward to commission the PVD cluster tool, finalise and optimise the test rigs, and integrate all work strands with our data management to then focus on developing technology-enabling materials for renewable energy applications.

ACKNOWLEDGEMENT

This Paper is funded by dtcc.bw – Digitalization and Technology Research Center of the Bundeswehr which we gratefully acknowledge [project Integrated Design Methodology for Advanced Functional Materials].

REFERENCES

- [1] J.B. Goodenough, Y. Kim, *Chem. Mater.* **22** (2010) 587.
- [2] W.T. Grubb, D.W. McKee, *Nature* **210** (1966) 192.
- [3] B. Hammer, J. Norskov, *Nature* **376** (1995) 238.
- [4] N.M. Markovic *et al.*, *Fuel Cells* **1**(2) (2001) 105.
- [5] A. Rabis *et al.*, *J. Phys. Chem. C* **118** (2014) 11292.
- [6] G. Greczynski, L. Hultman, *Prog. Mater. Sci.* **107** (2020) 100591.
- [7] L. Fabbrizzi, *ChemTexts* **6** (2022) 22.
- [8] A. Jain *et al.*, *APL Materials* **1** (2013) 011002.
- [9] G. Kresse, J. Hafner, *Phys. Rev. B* **47** (1993) 558; R. Dovesi *et al.*, *WIREs Comput. Mol. Sci.* **8** (2018) e1360; J.C.A. Pentece *et al.*, *J. Chem. Phys.* **152** (2020) 174111.
- [10] K. Mathew *et al.*, *Comput. Mater. Sci.* **139** (2017) 140.
- [11] A. Silva *et al.*, *NPJ Comput. Mater.* **8** (2022) 178.
- [12] A. Van der Ven, *An. Rev. Mater. Res.* **48** (2018) 27.
- [13] P. Chen *et al.*, *Nature* **420** (2002) 302.



FIGURES 10: CALCULATED ENERGY (LEFT AXIS) AND LATTICE VOLUME (RIGHT AXIS) PER COBALT ATOM AS A FUNCTION OF FRACTION OF TOTAL COBALT ATOMS IN A HIGH SPIN STATE. THE GREY AREA INDICATES THE 95% CONFIDENCE INTERVAL FOR THE QUADRATIC FIT TO THE CALCULATED ENERGY.

- [14] H. Cao *et al.*, *Prog. Nat. Sci.: Mater. Int.* **22** (2012) 550.
- [15] A. Santoru *et al.*, *Phys. Chem. Chem. Phys.* **18** (2016) 3910.
- [16] A. Santoru *et al.*, *Inorg. Chem.* **57** (2018) 3197.
- [17] R. Sakakibara *et al.*, *Sol. Energy Mater. Sol. Cells* **238** (2022) 111536.
- [18] Z. Wang *et al.*, *Sol Energy Mater. Sol. Cells* **238** (2022) 111554.
- [19] G. Krishnamurthy *et al.*, *Sci. Rep.* **11** (2021) 3330.
- [20] Y.H. Tan *et al.*, *ACS Nano* **12** (2018) 5856.
- [21] G. Gritzner, J. Kůta, *Electrochim. Acta* **29** (1984) 869.
- [22] F.A. Garcés-Pineda *et al.*, *Nat. Energy* **4** (2019) 519; X. Ren *et al.*, *Nat. Commun.* **12** (2021) 2608; T. Wu *et al.*, *Nat. Commun.* **12** (2021) 6251.
- [23] T. Kambara, *J. Chem. Phys.* **70** (1979) 4199; R. Zimmermann, E. König, *J. Phys. Chem. Solids.* **38** (1977) 779.
- [24] J. P. Perdew, Y. Wang, *Phys. Rev. B* **45** (1992) 13244.
- [25] <https://www.hsu-hh.de/hpc/en/hsuper-2/>.